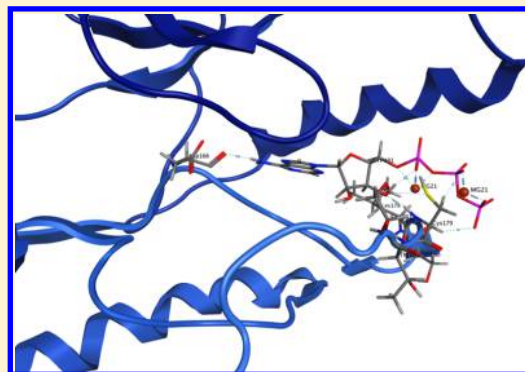


# Molecular Dynamics Studies of the Protein–Protein Interactions in Inhibitor of $\kappa$ B Kinase- $\beta$

Michael R. Jones, Cong Liu, and Angela K. Wilson\*

Department of Chemistry and Center for Advanced Scientific Computing and Modeling, University of North Texas, Denton, Texas 76203-5017, United States

**ABSTRACT:** Activation of the inhibitor of  $\kappa$ B kinase subunit  $\beta$  (IKK $\beta$ ) oligomer initiates a cascade that results in the translocation of transcription factors involved in mediating immune responses. Dimerization of IKK $\beta$  is required for its activation. Coarse-grained and atomistic molecular dynamics simulations were used to investigate the conformation–activity and structure–activity relationships within the oligomer assembly of IKK $\beta$  that are impacted upon activation, mutation, and binding of ATP. Intermolecular interactions, free energies, and conformational changes were compared among several conformations, including a monomer, two different dimers, and the tetramer. Modifications to the activation segment induce conformational changes that disrupt dimerization and suggest that the multimeric assembly mediates a global stability for the enzyme that influences the activity of IKK $\beta$ .



## ■ INTRODUCTION

Impeding activation of the nuclear factor (NF)- $\kappa$ B pathway has been a popular aim for designing new anti-inflammatory therapeutics for many disease states, including cancer, stroke, and viral infections.<sup>1</sup> The NF- $\kappa$ B complex is directly involved in regulating immune responses to a variety of stimuli and is composed of an assembly of five transcription activators<sup>2</sup> related by the presence of a distinctive Rel homology domain (RHD):<sup>3,4</sup> RelA (p65), RelB, c-Rel, p50/p105 (NF- $\kappa$ B1), and p52/p100 (NF- $\kappa$ B2).<sup>5–9</sup> Separated into two classes by C-terminal domains, the NF- $\kappa$ B subfamily proteins, p50/p105 and p52/p100, are not always transcription activators unless they form dimers with the Rel subfamily proteins, RelA, RelB, and c-Rel.<sup>10–17</sup> The RHD, responsible for dimerization and binding to DNA, contains the nuclear-localization sequence (NLS)<sup>18–20</sup> and the binding sites for inhibitors.<sup>21–23</sup>

Although there are various ways to signal activation of the NF- $\kappa$ B pathway, the inhibitory subunits I $\kappa$ B (I $\kappa$ B $\alpha$ , I $\kappa$ B $\beta$ , and I $\kappa$ B $\epsilon$ )<sup>5</sup> are responsible for sequestering the inactive state of NF- $\kappa$ B dimers in the cytoplasm by acting as a steric block against NLS functionality.<sup>24</sup> Liberation of NF- $\kappa$ B complex happens upon signaled-induced degradation of the I $\kappa$ B complex, thus mediating gene transcription; hence, inhibition of I $\kappa$ B activation is a promising target for anti-inflammatory drug development.<sup>24–29</sup> Enzymes responsible for this cascade of events have been linked to the catalytic subunits of I $\kappa$ B kinase (IKK),<sup>30–33</sup> specifically activation of the IKK $\alpha$  and IKK $\beta$  isoforms. Dual phosphorylation of the IKK $\alpha$  (at Ser176 and Ser180) and IKK $\beta$  (at Ser177 and Ser181) catalytic subunits regulate aberrant signaling pathways by which the activated subunits, both capable of undergoing autophosphorylation, phosphorylate I $\kappa$ B $\alpha$  at Ser32 and Ser26 and I $\kappa$ B $\beta$  at Ser19 and Ser23.

Both IKK $\alpha$  and IKK $\beta$  subunits, having a 52% sequence identity, contain a kinase domain (KD), leucine zippers (LZ), and helix–loop–helix (HLH) motifs that are capable of forming homo- and heterodimers.<sup>34</sup> Studies *in vitro* have shown that dimerization mediated by the LZ motifs regulates the activity and activation of KD by mutation of LZ and HLH motifs; although the HLH motif does not affect dimerization, it has been shown to contribute to KD activity.<sup>35</sup> Serine-to-alanine mutations in IKK $\beta$  prevent IKK activation, whereas in IKK $\alpha$ , autophosphorylation is deactivated but has no effect on IKK activity, highlighting IKK $\beta$  as an attractive target. Additionally, in the wild-type conformation of IKK $\beta$ , the position of the activation loop containing Ser177 and Ser181 hampers the docking of substrates into the pocket, whereas the activated conformation is more accessible as compared to the cyclic AMP-dependent kinase (cAPK).<sup>36</sup> This is mainly because the phosphorylation of the activation-loop residues causes a conformational change of the loop and even of the surrounding residues. This is an important phenomenon that suggests conformational change induced by these interactions plays an important role in bioactivity of the protein and medicinal chemistry. The activation loop also contains Cys179, which is known to be important for the phosphorylation of both IKK $\beta$  and IKK $\alpha$ . Studies have shown that modifications to the cysteine suppress activity of the enzyme and activation of the NF- $\kappa$ B pathway.<sup>37–40</sup>

With IKK $\beta$  being a key enzyme in activating the NF- $\kappa$ B pathway, the mechanism for inhibiting activation of IKK $\beta$  has remained elusive because of a lack of a tertiary-structural insight. The newly determined crystal structure of *Xenopus*

Received: December 6, 2013

Published: January 19, 2014

*laevis* IKK $\beta$  (xIKK $\beta$ ), having a gapless 74% sequence identity of human gene (hIKK $\beta$ ), was reported as a “dimer of dimers” in which dimerization was reasoned to be critical for activation rather than the activity for each homogeneous protomer.<sup>41</sup> Each protomer consists of 647 amino acids composed to form a kinase domain (KD) (residues 16–307), a ubiquitin-like domain (ULD) (residues 310–394), and a scaffold/dimerization domain (SDD) (410–666).

The presented structure of the kinase domain in xIKK $\beta$  does not resemble the active conformation upon comparison of the activation segments in available protein kinase crystal structures.<sup>42</sup> The activation segments are defined by a primary sequence beginning adjacent to a  $\beta$  sheet at a conserved DFG (Asp-Phe-Gly) triad and extends to a conserved APE (Ala-Pro-Glu) motif near an  $\alpha$  helix. Although the random coils share a consistent fold between the two motifs, the activation loop is diverse in both sequence and conformation unique to its protein–protein interactions and regulation. The activation segment in the xIKK $\beta$  structure begins at Asp166 and ends at Glu192, where Ser177–Ser181 (SXXXS) contains residues shown critical for activation. Although the KD contains the mitogen-activated protein (MAP) kinase<sup>43–46</sup> for serine phosphorylation, the SDD regulates activation via maintaining dimerization. Mutagenesis studies showed that wild-type IKK $\beta$  is a dimer, whereas the mutant is a monomer with a weaker affinity for dimerization, and upon mutation of Leu654 and Trp655 in the SDD, dimerization was lost.<sup>41</sup>

Previous computational and experimental work with IKK $\beta$  and similar Ser/Thr/Tyr kinases has revealed that the allosteric adenosine triphosphate (ATP) binding cavity is near the hinge connecting the N and C lobes of the kinase domain.<sup>41,42,47–51</sup> Comparative homology modeling of the monomer of IKK $\beta$  suggested that the KD is flexible, and allosteric ATP binding conformational changes were not easily observed using 80 ns simulations without the crystal structure.<sup>47,52</sup>

In this study, molecular dynamics (MD) simulations of IKK $\beta$  are presented that offer a greater insight on how conformational changes and protein–protein interactions within a multimeric assembly are influenced by distal modifications in the interacting subunits of IKK $\beta$ . Using a multiscale approach, coarse-grained modeling offers a reduced representation useful for predicting large-scale conformational changes, whereas atomistic simulations provide a more descriptive insight on activity; together, these approaches help discern dimerization disruption.

## COMPUTATIONAL METHODS

**System Preparation.** The initial coordinates for eight phosphomimetic mutant (S177E/S181E) molecules of xIKK $\beta$  were obtained from the Protein Data Bank<sup>53</sup> (PDB ID: 3QA8).<sup>41</sup> Combinations of the eight molecules were constructed to model multiple sets of tetramers, trimers, and dimers while using a monomer as a control (Table 1, Figure 1). Missing atoms on the side chains of Val79, Asp90, and Asp291

**Table 1. Summary of Modeled Systems**

model	chain
tetramer	ABCD, DEFG, BCEH
trimer	ABC, BCE
dimer	AB, AD, BE
monomer	A

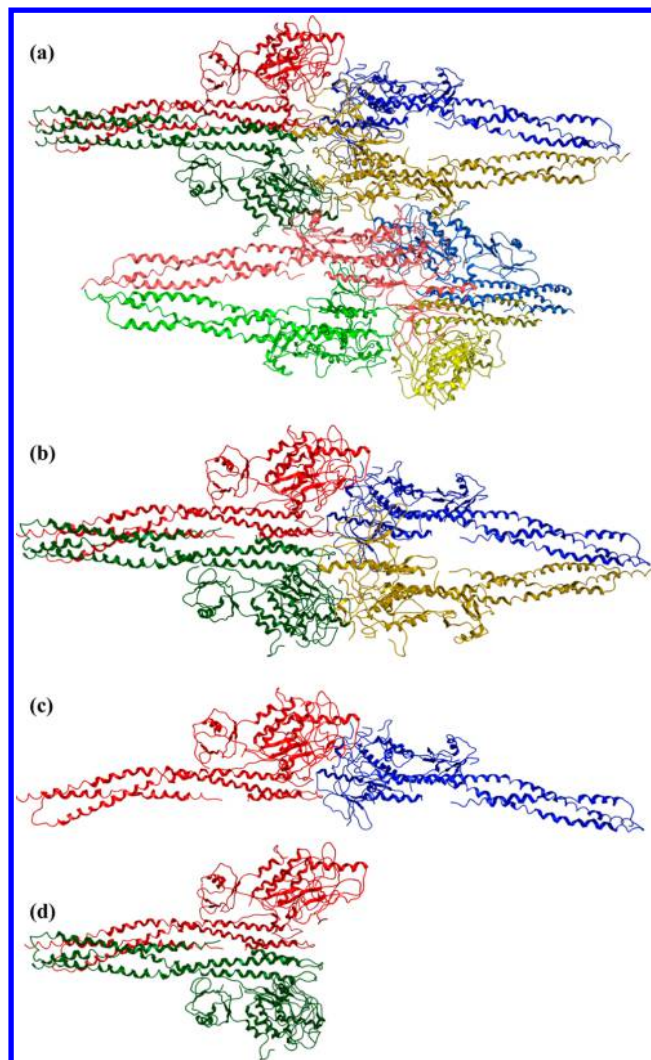


**Figure 1.** Representation of the models. The crystal structure was solved with eight identical molecules (a) forming two “dimer of dimers”, a tetrameric complex (b). Although a dimer is defined as the AB form (d), the alternative dimer, AD (c), has significance for structure stability.

were added using Molecular Operating Environment v.2011.10 (MOE).<sup>54</sup> Coarse-grained models (all models shown in Table 1) were protonated using MOE and minimized using the Amber99 force field.<sup>55,56</sup> Models for the atomistic simulations (AB and AD dimers and monomer) were prepared using the Leap module of AmberTools12.<sup>57,58</sup> The Site Finder application in MOE was used to investigate potential sites for ligand docking. Contact sites and propensity for ligand binding (PLB) indices<sup>59</sup> were used to compare both allosteric and nonallosteric ATP binding sites. ATP coordinated with Mg<sup>2+</sup> ions was extracted from a crystal structure of the Vgrg protein (PDB ID: 4DTH)<sup>60</sup> and docked using MOE with the induced-fit method positioning the adenine head toward the hinge (DFG motif) and the tail near the phosphoacceptor serines using the same starting position for all models (Figure 2). Ligand parameters were retrieved from the AMBER parameter database<sup>61</sup> and were set up using GAFF.<sup>62</sup> Parameters for phosphoserine<sup>63</sup> mutants (S177/181pS) were retrieved from Leap.

**Simulation Protocol.** To observe large, dynamical conformational changes, coarse-grained simulations were

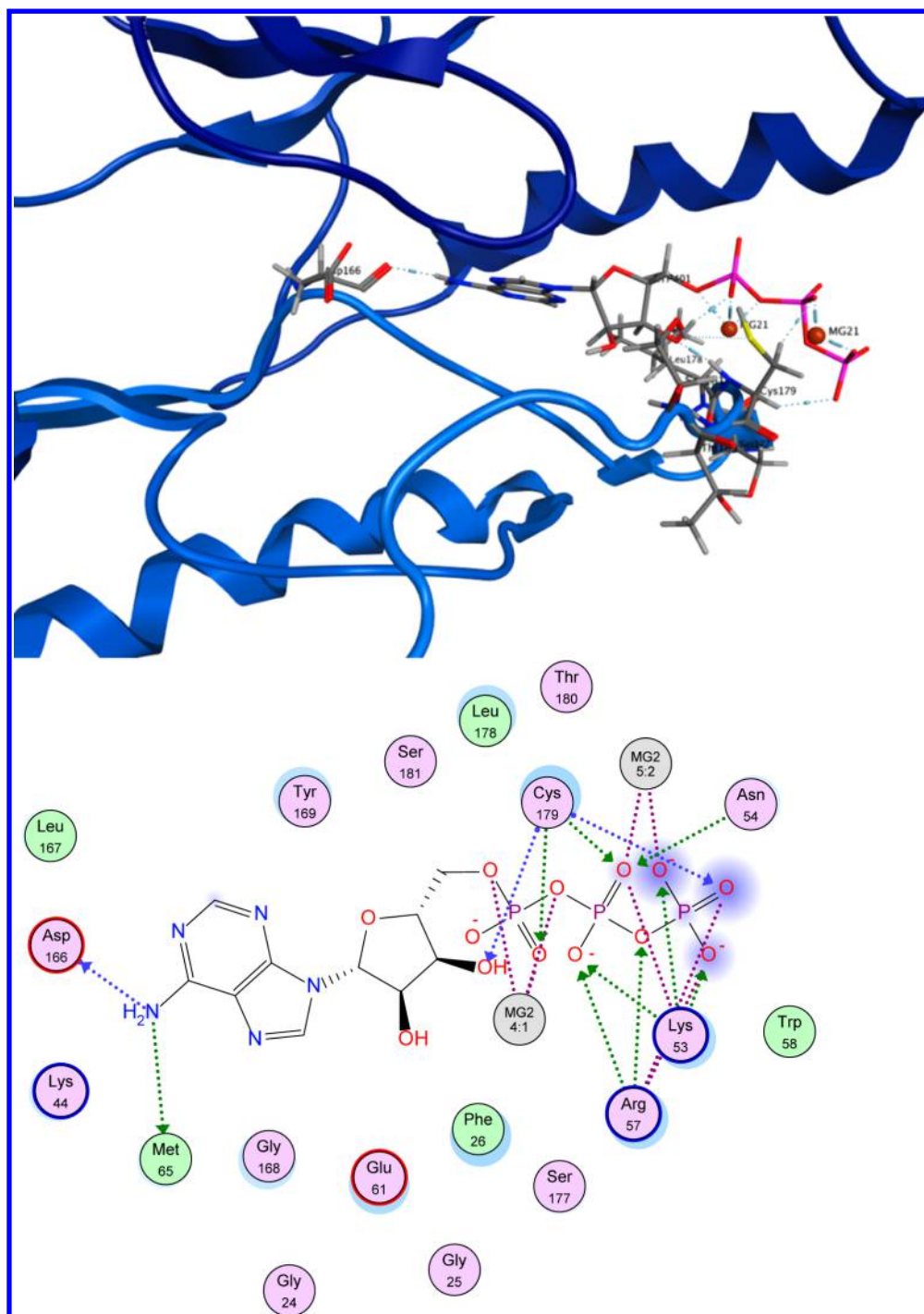


**Figure 2.** Characterization of the ATP/Mg<sup>2+</sup> docking cavity. The ATP ligand is positioned in the mouth of the activation loop (top). The adenine head of ATP is pointed toward Asp166, and the phosphate tail is outside of the pocket. The binding pocket is outlined and described by colored circles (purple and green) representing surrounding amino acids (bottom); the different outlines on the purple circles contrast the different types of polar side chains. Blue and green arrows indicate side chain and backbone acceptor–donors, respectively. The blue spheres surrounding the phosphate tail represent the pocket exposure, whereas the lighter-blue spheres highlight the receptor's exposure.

carried out for 50 ns at 300 K using CafeMol 2.0<sup>64</sup> with the AICG2 model accounting for nonlocal intrachain interaction (electrostatic, repulsion, and hydrophobic interactions). Atomistic simulations were performed for 10 ns at 300 K and 1 atm using AMBER 11 in the presence of 100 mM sodium chloride<sup>65</sup> and 10 Å of SPC/E<sup>66</sup> water beyond the solute in a cuboid box under the Amber99SB<sup>67</sup> force field. Prior to simulation, each solvated system was gradually relaxed under the NVT ensemble

by six minimization procedures (500 cycles of steepest-descent minimization followed by 500 cycles of conjugate-gradient minimization) with decreasing restraints on the protein of 500.0, 200.0, 20.0, 10.0, and 5.0 kcal/(mol Å<sup>2</sup>) per procedure to no restraints and then heated to 300 K over 100 ps. The baths were maintained using the isotropic position scaling protocol and the Langevin thermostat with the SHAKE algorithm.



Table 2. Binding Cavities Near the Activation Segment<sup>a</sup>

site	alpha spheres	contact atoms	amino acids	PLB index	residues
2	118	270	171	2.37	Leu186, Leu189, Ala190, Pro191, Glu192, Leu193, Trp206, Pro221, Phe222, Asn225, Gln227, Gln230, Trp231, His232, Gly233, Lys234, Val235, Ile243, Val244, Val245, Tyr246, Asp247, Asp248, Leu249, Thr250, Val253, Phe255, Ser256, Ser257, Leu277, Gln278, Leu281, Met282, Trp283
3	87	200	122	1.53	Gly22, Thr23, Gly24, Gly25, Arg144, Asp145, Leu146, Lys147, Glu149, Asp166, Leu167, Tyr169, Thr180, Phe182, Val183, Gly184, Thr185, Leu186, Gln187, Tyr188, Leu189, Glu192, Leu194, Glu195, Tyr199, Ser207
6	35	115	76	0.64	Glu61, Ile64, Met65, Lys66, Leu68, Asn69, Val73, Val74, Ser75, Met96, Tyr135, Leu136, Ile141, His143, Ile164, Ile165, Leu167, Gly168, Ala170
10	40	103	68	0.32	Leu21, Gly22, Val29, Tyr98, Cys99, Glu100, Gly101, Gly102, Asp103, Lys106, Glu149, Asn150, Val152, Ile165, Asp166

<sup>a</sup>Column 2 characterizes the number of alpha spheres identified within the cavity. Quantities in columns 3 and 4 denote the number of contact atoms and amino acids surrounding the cavity, respectively. The PLB index ranks the concavity in increasing order.

**Trajectory Analysis.** Trajectory analysis was performed using CafeMol and AMBER 11 for coarse-grained and atomistic simulations, respectively, and visualized in Chimera<sup>68</sup> and VMD.<sup>69</sup>

**Simulation Stability.** Simulation parameters were extracted from the trajectories and plotted to access atomistic simulation stability. Root-mean-square deviation (RMSD) values from the starting structure were performed using the PTRAJ module of the Amber suite to investigate flexibility and conformational changes.

**Hydrogen-Bonding Analysis.** Hydrogen-bonding analyses were performed with the CPPTRAJ module of AmberTools, where a hydrogen bond was defined by a cutoff distance of 3.5 Å and a donor-hydrogen-acceptor angle of 180 ± 60°.

**Energetic Analysis.** Free-energy calculations were carried out using the MMPBSA.py<sup>70</sup> module with AmberTools and AMBER 11. The electrostatic solvation energy was calculated for every picosecond over a span of 10 ns using three Generalized Born (GB) models: the pairwise GB models of Hawkins and co-workers (GB-HCT)<sup>71–73</sup> and two modified models developed by Onufriev and co-workers (GB-OBC1 and GB-OBC2),<sup>74</sup> setting dielectric constants to 1 and 80 for the interior and exterior of the molecule, respectively. Because relative free energy trends were of interest, solute entropy was neglected.<sup>75</sup> Additionally, the PISA (Protein Interfaces, Surfaces, and Assemblies) procedure<sup>76</sup> was used to predict the free energy of formation and dissociation of the two dimeric assemblies studied.

## RESULTS

**Docking is Aesthetic.** Potential binding sites for ligands were investigated using the Site Finder application in MOE to observe the accessible binding sites from the static tetrameric assembly (A, B, C, and D represent four protomers in xIKKβ, respectively). Approximately 46 accessible cavities were found in a single protomer; only four of the predicted sites have contacts with the activation segment (Table 2). Sites 2, 3, 6, and 10 have pockets containing 103–270 contact atoms and a wide range of PLB scores. PLB indices are ranked on concavity in which the highest PLB index would be considered to be the most probable ligand-binding site.<sup>59</sup> The largest pocket is shown in site 2 (Figure 3). Site 2 is stationed at the bottom of the kinase domain in a cavity that includes the APE motif as contact atoms. Deeper into the pocket of the activation loop, sites 3 and 6 both reach toward the hinge of the N and C terminus and include the DFG triad. Both sites are within a reasonable proximity (≤5.0 Å) of the SXXXS sequence. Site 10

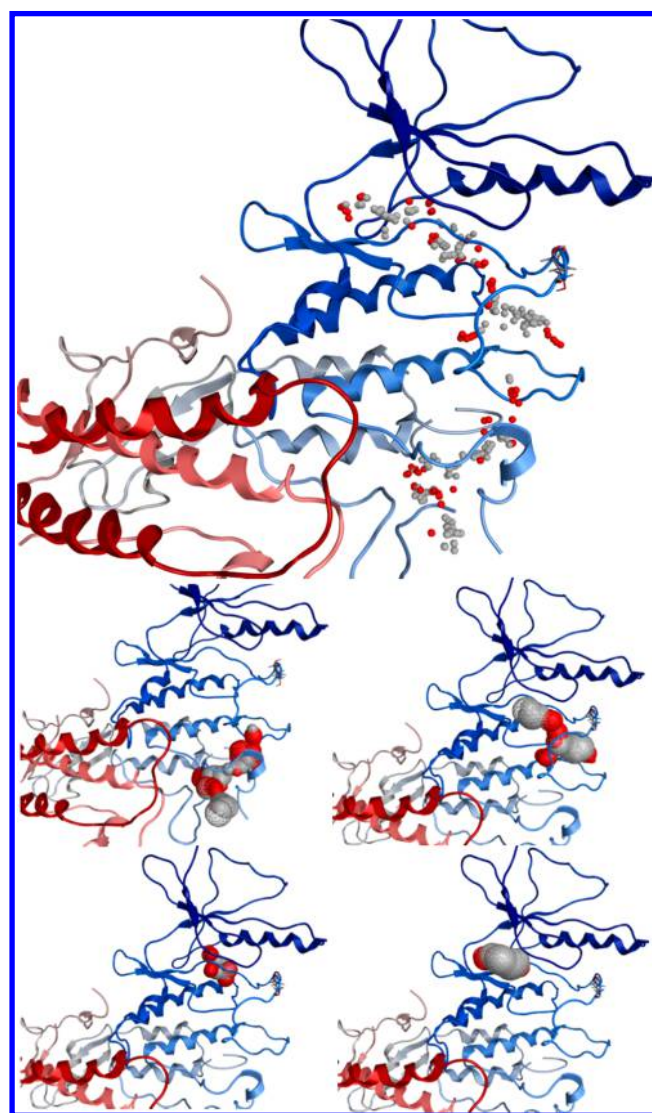


**Figure 3.** Visualization of the predicted cavities. All alpha spheres are shown for the four sites (top). The red and white spheres indicate hydrophilic and hydrophobic cavities, respectively. Wire-frame representations of the four sites are shown individually: site 2 (middle left), site 3 (middle right), site 6 (bottom left), and site 10 (bottom right).

is also in the hinge region and corresponds to an allosteric binding region. The only adjacent contact atom pertinent to the activation segment is Asp166 of the DFG triad. These

Table 3. Summary of Dimer Assembly Energetics<sup>a</sup>

model	AB dimer					AD dimer				
	$A_{\text{BSA}}$	$\Delta G^{\text{int}}$	$\Delta G^{\text{diss}}$	$T\Delta S^{\text{diss}}$	$P_v$	$A_{\text{BSA}}$	$\Delta G^{\text{int}}$	$\Delta G^{\text{diss}}$	$T\Delta S^{\text{diss}}$	$P_v$
WT	1614.2	−21.9	9.5	15.7	0.061	440.0	1.3	−14.9	15.6	0.801
S177/188E	1614.2	−21.9	9.5	15.7	0.061	440.0	1.3	−14.9	15.6	0.801
S177/188pS	1783.7	−14.9	1.5	17.2	0.207	615.8	−3.0	−12.1	17.1	0.491

<sup>a</sup>Determined with PISA. The buried surface between the engaged interfaces ( $A_{\text{BSA}}$ ) is reported in Å<sup>2</sup>. The  $P$  value ( $P_v$ ) indicates the probability of finding a more hydrophobic interface (lower  $P_v$  values indicate fewer hydrophobic sites). The dissociation free energies ( $\Delta G^{\text{diss}}$ ) and binding free energies ( $\Delta G^{\text{int}}$ ) are reported in kcal/mol.

accessible pockets within the structure gave rise to the proposal of a nonallosteric docking pose for ATP.

**Dimer Stability of the Crystal System.** Using the static conformations of the initial ligand-free dimer models, theoretical predictions on the dimer assemblies were calculated using PISA. The free energy of binding,  $\Delta G^{\text{int}}$ , is used to describe the free energy of interface formation between subunits, whereas the free energy of change upon dissociation,  $\Delta G^{\text{diss}}$ , corresponds to the difference between the associated and dissociated structures.<sup>76,77</sup> In these approximations, a negative  $\Delta G^{\text{diss}}$  value indicates that the structure is thermodynamically unstable and would readily dissociate and a positive value suggests a more stable assembly in which an external component would need to be added to induce dissociation. The results shown in Table 3 indicate that the AB dimer is more tightly bound than the AD dimer for the WT and S177/188E models. In contrast, the S177/181pS model has a weaker binding free energy in the AB dimer and a stronger binding affinity in the AD dimer. Additionally, both the WT and S177/188E models have larger  $\Delta G^{\text{diss}}$  values than the S177/181pS model in the AB dimer but smaller values in the AD dimer. This indicates that the S177/181pS model is less thermodynamically stable in the AB dimer and more thermodynamically stable in the AD dimer than the WT and S177/188E models. Although predictions for the WT agree with experimental observations, identical values for the WT and S177/181E models were predicted for both the AB and AD dimers, highlighting an inherent weakness in the parametrization of the PISA procedure.<sup>76</sup> This method may not always be useful for predicting the conformational stability for protein–protein interactions using static structures.

**Coarse-Grained Simulations.** All coarse-grained models were simulated for 50 ns to gain qualitative insight about the significance of simulating multiple protomers that may contribute to the conformational stability of the xIKK $\beta$  assembly. The RMSD calculated from the starting structure was compared against the multiple models shown in Table 1 and scaled to fit a monomer (Figure 4). Although calculating RMSD from the starting structure is one way to determine the stability of the structure, the dynamics in flexible regions can yield misleading RMSDs. Each model exhibits continuous increases in the deviation, indicating sustained conformational changes. In these simulations, the continuous structural changes occurred in the kinase domain. Qualitatively, throughout the simulation, the activation loop of the kinase domain periodically opened and closed, suggesting that its structural flexibility may play a role in regulating molecular traffic in the activation loop. In terms of comparing conformational stability among the different models, it is apparent within the first 25 ns that there is conformational favorability, specifically fewer fluctuations in the assembly, for models containing multiple protomers. The monomer was the least stable system in these simulations

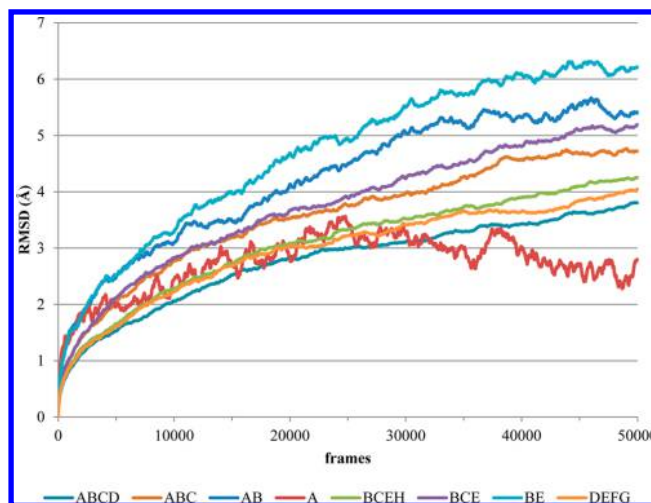


Figure 4. RMSD plots for the different assemblies using coarse-grained MD. Frames were plotted for every 1 ps for a total of 50 000 frames (50 ns).

because it began to denature within the first 25 ns of the simulation; thus, RMSD after 25 ns were ignored. Although coarse-grained time scales cannot be directly compared with atomistic time scales, this demonstrates the influence that the assembly of a complex has on the mobility of individual protomers on short time scales.

**Atomistic Simulation of Dimers and Monomer.** To characterize the significance and relationship between kinase domain activity and dimerization, atomistic simulations were carried out for 10 ns for two sets of dimers, and the monomer was observed as a control. Simulation stability was assessed by monitoring thermodynamic parameters (Table 4) from the starting and average structures. Average total energies, densities, and temperatures were compared among the different morphs of the monomer and dimers. Properties of each monomer, AB dimer, and AD dimer were comparable among the WT, S177/181E, WT-ATP, and S177/181pS models, indicating that each monomer and dimer structures, respectively, maintained the defined simulation parameters. The RMSD values for the 12 starting structures shown in Figure 5 reveal variations of conformational flexibility throughout the 10 ns simulations. For the monomer, the WT has much more structural fluctuations than the mutant and ATP-bound models. For the dimers, the WT, WT-ATP, and S177/181pS models have more comparable RMSD values than the S177/181E model. In the WT-ATP model, the flexibility of the activation loop is minimized because of electrostatic interactions with the nonallosteric bound ATP. From this data, it is indicative that the flexibility of the activation segment in the kinase domain contributes little toward the larger fluctuations observed in the full structure of

Table 4. Averaged Thermodynamic Data for the 10 ns Atomistic MD Simulation<sup>a</sup>

	model	$E_{\text{tot}}$	$\sigma$	rho	$\sigma$	T	$\sigma$
WT	monomer	-371 875.0	398.6	1.0362	0.0008	300.0	0.9
	dimer: AB	-448 514.1	528.9	1.0530	0.0009	300.0	0.8
	dimer: AD	-880 796.6	651.6	1.0222	0.0005	300.0	0.6
S177/188E	monomer	-371 885.3	400.0	1.0362	0.0008	300.0	0.9
	dimer: AB	-460 262.3	531.5	1.0513	0.0009	300.0	0.8
	dimer: AD	-880 880.4	652.1	1.0221	0.0005	300.0	0.6
WT-ATP	monomer	-373 339.9	394.6	1.0364	0.0007	300.0	0.9
	dimer: AB	-448 774.7	524.0	1.0528	0.0010	300.0	0.8
	dimer: AD	-881 975.2	659.6	1.0226	0.0005	300.0	0.6
S177/181pS	monomer	-372 369.3	396.6	1.0363	0.0007	300.0	0.9
	dimer: AB	-447 724.1	519.1	1.0521	0.0009	300.0	0.8
	dimer: AD	-881 267.0	657.1	1.0221	0.0005	300.0	0.6

<sup>a</sup>The total energy ( $E_{\text{tot}}$ ), density (rho), and temperature (T) per system are reported in units of kcal/mol, g/mL, and kelvin, respectively, next to the standard deviation ( $\sigma$ ).

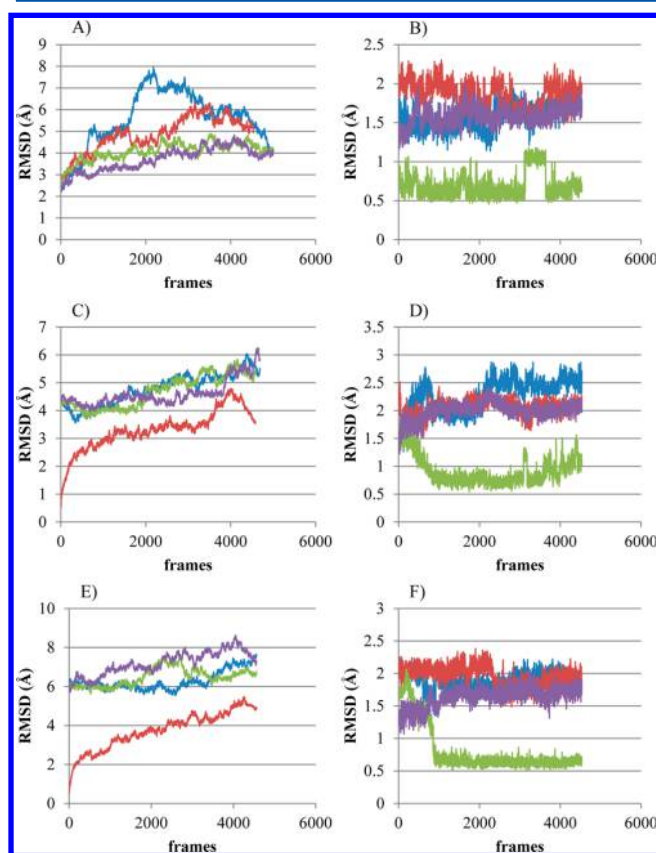


**Figure 5.** RMSD from the starting structure for the 10 ns simulation. The different RMSDs of the monomer (a,b), AB dimer (c,d), and AD dimer (e,f) are colored accordingly (blue, WT; red, S177/181E; green, WT-ATP; and purple, S177/181pS). Plots A, C, and E represent the RMSD of the entire structure, whereas the plots B, D, and F represent only the activation segment of the principle monomeric chain. Frames were plotted for every 2 ps for a total of 5000 frames (10 ns).

the dimers, indicating that the observed structural changes occur in other parts of the complexes.

**Hydrogen Bonding between Dimer Interfaces.** Structure-based mutagenesis and ultracentrifugation studies investigating SDD mediated dimerization established that the wild type is a dimer, whereas upon mutation of Leu654, Trp655, and Leu658, dimerization failed. To quantify the loss in dimerization upon activation of the complex, a hydrogen-

bond analysis was performed. Hydrogen-bonding patterns in the AB dimer includes series of both charged and uncharged amino acids including Glu, Asp, Gln, Ser, and Leu. Activation by both phosphomimetic mutation and phosphorylation leads to a decrease in hydrogen-bond occupancy throughout the simulation. Specifically, Glu576, Ser489, Asp493, Gln478, Glu565, and Leu658 of one protomer maintain hydrogen bonds with the opposing protomer for 50 to 100% of the simulation for the wild-type; however, these hydrogen-bond occupancies decrease in the activated species (Table 5). The AD dimer (Table 6), however, does not follow a similar trend, which is due to the distances between the dimer interface. Occupancies for the WT-ATP models failed to follow a trend readily comparable with the other models; however, it is clear that the docking of ATP has the ability to disrupt SDD-mediated dimerization.

**Binding Free Energies.** Calculating the average binding free energy using GB approximations can provide relative trends of free energies of association and dissociation. All binding free energies are shown in Table 7. Using the pairwise descreening approach (HCT), the dimerization of the AB model is less favorable upon mutation of S177/181. Although the phosphomimetic mutations show a weaker binding-affinity trend than the phosphoserine model, the phosphoserine dimer does begin dissociating (Figure 6). In contrast, the AD model has a stronger binding affinity upon active rendering with similar exaggerations from the phosphomimetic mutation. This relative trend, visualized in Figure 7, supports the favorability for dimerization in the wild type but also proposes an affinity shift toward the AD dimer upon activation. Observing the OBC models, the trend is consistent, excluding the phosphomimetic mutant with the OBC2 model. For the AB dimer containing ATP, only the HCT model was used to calculate  $\Delta G^{\text{bind}}$  between the dimer interfaces to investigate how ATP binding affects dimerization. The results show that ATP, as expected, prompts dissociation.

## DISCUSSION

Different structure-guided approaches to drug discovery have been developed over the years to guide rational design better.<sup>78–81</sup> MD simulations are widely used to elucidate structure–activity relationships; however, these approaches have their own weaknesses because of inadequate conformational sampling, which can be due to high computational costs and inherent weaknesses within the force-field parametriza-



Table 5. Hydrogen-Bonding Occupancies for the AB Dimer Interface<sup>a</sup>

(AB) WT			(AB) S177/181E			(AB) WT-ATP			(AB) S177/181pS		
Y	X–H	O	Y	X–H	O	Y	X–H	O	Y	X–H	O
Glu576	Arg573	99	Glu576	Arg573	71	Arg650	Gln651	84	Glu565	Arg568	70
Ser489	Gln651	96	Asp569	Arg572	68	Asp546	Arg460	71	Lys482	Lys482	59
Glu576	Arg572	89	Ser489	Gln651	57	Trp655	Tyr497	50	Lys482	Phe485	53
Tyr497	Gln651	81	Asp493	Gln651	53	Gln478	Gln478	36	Asp493	Gln652	45
Asp546	Arg460	75	Asp493	Gln652	50	Ser489	Glu648	31	Asp493	Trp655	36
Asp493	Gln652	63	Ser489	Gln652	45	Phe485	Phe485	29	Phe485	Phe485	33
Gln478	Gln478	55	Glu19	Arg592	39	Phe485	Gln647	26	Gln651	Gln651	31
Glu565	Arg438	52	Phe485	Phe485	29	Gln500	Lys659	26	Glu648	Ser488	30
Leu658	Leu658	49	Gln110	Gln566	28	Phe486	Gln651	22	Phe485	Lys482	29
Trp655	Gln500	39	Glu502	Arg666	25	Ala481	Lys482	22	Trp655	Tyr497	28
Arg573	Arg572	36	Lys482	Phe485	22	Trp268	Gln651	22	Phe503	Cys652	28
Glu464	Thr463	36	Glu19	Asn588	21	Asp484	Lys482	22	Ala481	Lys482	27
Trp655	Tyr497	34	Gln548	Gln548	21	Ala481	Gln478	19	Phe485	Phe486	25
Lys659	Gly504	29	Gly504	Trp655	21	Lys482	Phe485	19	Gln478	Gln478	23
Arg573	Arg573	28	Ala481	Lys482	19	Lys482	Lys482	16	Ser357	Gln548	23
Glu648	Ser489	27	Phe503	Arg666	18	Leu654	Trp655	16	Trp655	Asp493	21
Pro578	Glu576	26	Glu19	Arg419	17	Phe485	Lys482	16	Asp493	Gln651	20
Lys467	Lys467	26	Trp655	Lys496	17	Phe486	Phe485	14	Ser489	Gln651	20
Asp569	Arg572	26	Gln548	Arg452	16	Phe485	Phe486	14	Asp569	Arg568	19
Cys662	Phe503	25	Glu648	Phe485	16	Gln652	Lys496	14	Phe485	Glu648	18
Glu502	Ser653	24	Ser619	Phe503	15	Gln500	Trp655	13	Ala481	Gln478	17
Gln500	Trp655	23	Lys482	Lys482	15	Ile490	Gln651	12	Lys467	Lys467	16
Lys482	Phe485	18	Gln110	Leu570	15	Ser489	Gln651	11	Arg549	Ser357	16
Ala481	Lys482	18	Gln478	Gln478	14	Phe485	Glu648	11	Glu16	Arg419	16
Lys482	Ala481	17	Gly504	Lys659	13				Leu658	Leu658	15
									Lys659	Tyr497	14
									Ser489	Glu648	13
									Phe503	Arg666	13
									Gln500	Lys659	13
									Arg573	Arg572	13

<sup>a</sup>In each model, an acceptor (Y) and a donor (X–H) were defined and analyzed throughout the 10 ns simulation. The percent occupancy (O) represents the fraction of frames in which a bond was observed.

Table 6. Hydrogen-Bonding Occupancies for the AD Dimer Interface<sup>a</sup>

(AD) WT			(AD) S177/181E			(AD) WT-ATP			(AD) S177/181pS		
Y	X–H	O	Y	X–H	O	Y	X–H	O	Y	X–H	O
Asn225	Leu223	97	Thr250	Trp226	78	Asp536	Arg582	59	Asp536	Arg579	88
Leu193	Thr250	84	Asp536	Arg579	55	Asp536	Arg579	49	Pro228	Thr250	53
Thr250	Trp226	82	His232	Trp231	39	Asp248	Trp226	25	Pro224	Asn225	45
His232	Val229	38	His232	His232	39	Pro417	Gln48	21	Leu249	Leu194	40
Asn225	Phe222	29	Pro224	Asn225	35	Asn225	Trp226	20	Asp248	Leu193	34
Pro228	Asp248	29	Arg577	Arg582	35	His232	Trp226	16	Pro578	Arg579	29
Gly251	Trp226	27	Glu49	Arg592	23	Trp226	Tyr423	15	Thr250	Trp226	28
His232	Trp231	22	Pro224	Pro228	20	Leu384	Ser181	14	Pro228	His232	28
Pro228	Asp247	19	Thr250	Gln227	19	Trp231	Trp231	12	Trp226	His425	27
Trp226	Tyr423	18	Arg236	Pro228	19	Gln227	Thr250	10	Pro228	Asp248	25
Trp226	Phe255	17	Gln230	Val229	18	Leu193	Leu249	10	Ser257	Pro228	17
Asn225	His425	16	Thr424	Asn225	18	Trp231	His232	9	Thr250	Gln227	15
Pro224	Pro224	15	Arg579	Arg582	17	Pro578	Arg579	7	Leu249	Glu195	13
Asn225	Pro224	14	Val183	Thr422	17				Trp226	Tyr423	13
Leu384	Trp226	13	Asp248	Pro228	14				Thr250	Leu194	12
Val183	Leu421	12	Glu49	Arg419	13				Sep181	Lys418	9
Phe255	Trp226	11	Arg582	Arg582	13				His232	Val229	9
Thr250	Gln227	10	Asn225	Val229	12						
			Leu186	Thr250	10						

<sup>a</sup>In each model, an acceptor (Y) and a donor (X–H) were defined and analyzed throughout the 10 ns simulation. The percent occupancy (O) represents the fraction of frames in which a bond was observed.

Table 7. Binding Free Energies

model		kcal/mol		
		HCT	OBC1	OBC2
WT	AB	−180.7	−88.6	−50.3
	AD	−74.6	−41.6	−25.8
E177/181	AB	−153.7	−65.5	−30.4
	AD	−93.9	−51.0	−35.0
pS177/181	AB	−168.5	−82.4	−39.5
	AD	−69.5	−28.2	−13.4
WT-ATP	AB	−122.0		

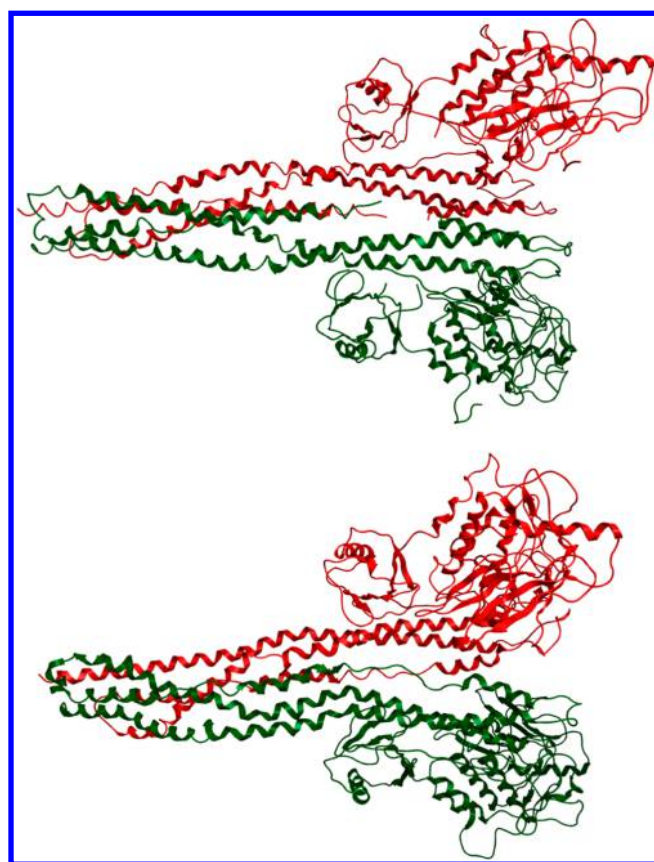


Figure 6. Comparison of the phosphorylated AB dimer. Shown are the starting structure (top) and final structure (bottom) after 10 ns.

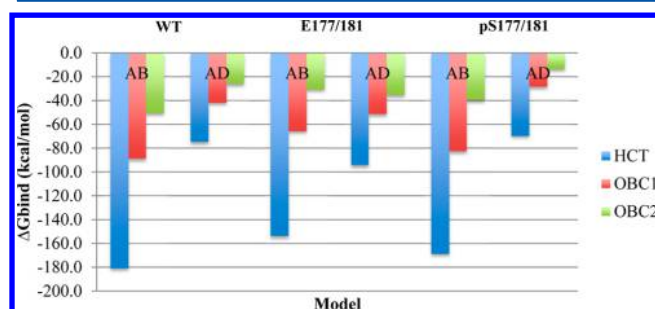


Figure 7. Comparison of binding free-energy trends with the HCT, OBC1, and OBC2 models.

tions.<sup>79,82,83</sup> Focusing on the limitation of conformational sampling, coarse-grained techniques have been designed to provide reduced representations that permit investigations of various conformational states of large biomolecular systems and assemblies with longer time scales<sup>84,85</sup> that provide a

foundation for multiscale modeling approaches. Typically, molecular dynamics simulations of protein–ligand recognition are studied using noncovalently bound ligands to a single subunit or domain of a protein, often neglecting the protein's contribution to the quaternary structure. Although these free, unbound ligands are unable to induce a change in effective force constants or break bonds with point-charged-based force fields, they do induce sterics that can make changes in the local tertiary structure. Despite the limits to conformational sampling, it is important to study the multiple protomers or subunits of quaternary structures when investigating the impact of ligand binding or point mutations to avoid misleading details describing the recognition events, especially those of systems containing homomultimeric subunits.

As shown in this work, it is important to consider the full structure of IKK $\beta$  for the study of the effects of distal modifications. The assembly of the inactive xIKK $\beta$  is described as a symmetric stationary assembly, whereas upon activation, the quaternary structure dissociates from the central configuration. From the coarse-grained simulation, the large-scale motions of the kinase domain are pertinent to the kinase activity in that the activation loop symbolizes a pair of lips that opens and closes repeatedly during the MD simulation. This 'open' and 'closed' conformation resembles the backbone flexibility experimentally shown in the cAMP-dependent protein kinase (cAPK or PKA) catalytic subunit.<sup>86,87</sup> A central location for potential conformational dynamics is at the hinge; thus, opening of the hinge makes the possibility for ligand entrance in the lips of the KD possible in both conformational states. Because of the orientation of the dimer–dimer interface, the activation loop was unhindered and accessible. The accessibility of the hinge through the activation loop in the crystal structure is tight but accessible for flat structures, such as ATP. The functional groups contained within the pocket of the activation loop create a polar cavity, which favors the formation of hydrogen bonds. Noncovalent binding of ATP in the binding pocket made an impact on the dimerization. From this docked ATP position, the role of Cys179 in modulating ATP binding and activation can be described as a side chain that aids in holding ATP in the pocket.

Since the publication of the xIKK $\beta$  crystal structure, two structures have been solved for the active conformation of hIKK $\beta$ .<sup>88,89</sup> Both studies confirm that the overall modular arrangement of the different domains between hIKK $\beta$  and xIKK $\beta$  are consistent. Additionally, both of the crystal structures confirm that the active assembly of IKK $\beta$  resembles a pair of opening shears; this is in agreement with our simulation data. Despite the subtle differences of the opened and closed conformations, the activation segment of the KD regulates activity and dynamics. Modifications to the distal activation loop made a significant impact to the dimerization within a short simulation time. Although the atomistic simulation time was not long enough to observe the opened and the closed conformations, we saw that the pocket from the KD began to open throughout the 10 ns simulation across all models. The phosphomimetic and phosphoserine mutations formed hydrogen bonds and salt interactions with the solvent and nearby side chains; however, the occupancies of these interactions were not maintained, which suggests an entropic flexibility of the KD. Previous investigations of IKK activity showed that IKK $\beta$  activity can be expressed with phosphomimetic mutations.<sup>32</sup> In agreement with experiment, the effects of imploring phosphomimetic mutations rather than actual



phosphorylated amino acids were observed in these simulations. Although the opened conformation resembles the active kinase, the inactive KD shows similar activity.

## CONCLUSIONS

In this study, molecular dynamics simulations were employed to investigate conformational stability for modeling multimeric species and to decipher whether dimerization is interrupted upon activation of IKK $\beta$ . Coarse-grained MD simulations showed that simulating more than one protomer of the multimeric assembly provided greater stability for the assembly of IKK $\beta$ . Interactions at the dimer–dimer interface between the SDD and KD promote a conformational stability for the inactive state of IKK $\beta$ . Atomistic simulations of the two dimer models confirmed that each protomer mediates electrostatic interactions that are responsible for activity of IKK $\beta$ . Dimerization of IKK $\beta$  is disrupted upon activation of Ser177 and Ser181. Rather than inducing local conformational changes within the KD observable within the 10 ns simulation, binding of ATP induces conformational changes that disrupt dimerization. Additionally, phosphomimetic mutations can adequately express the active state of IKK $\beta$ .

Regarding the molecular modeling of IKK $\beta$  activity, we highlight the importance of considering both conformation–activity and structure–activity relationships. Considering how protein–protein interactions within assemblies are affected when docking ligands or modifying protein side chains is critical for understanding structure–activity relationships, even in sites distal from the protein–protein interface. Significant structure–activity relationships can be underestimated by neglecting protein–protein interactions.

## AUTHOR INFORMATION

### Corresponding Author

\*E-mail: akwilson@unt.edu; Fax: (940) 565-4318.

### Notes

The authors declare no competing financial interest.

## ACKNOWLEDGMENTS

We gratefully acknowledge the High Performance Computing Services at the University of North Texas.

## REFERENCES

- (1) Baldwin, A. S., Jr. Series introduction: The transcription factor NF- $\kappa$ B and human disease. *J. Clin. Invest.* **2001**, *107*, 3–6.
- (2) de Martin, R.; Schmid, J. A.; Hofer-Warbinek, R. The NF-kappaB/Rel family of transcription factors in oncogenic transformation and apoptosis. *Mutat. Res.* **1999**, *437*, 231–243.
- (3) Ghosh, S.; May, M. J.; Kopp, E. B. NF-kappa B and Rel proteins: Evolutionarily conserved mediators of immune responses. *Annu. Rev. Immunol.* **1998**, *16*, 225–260.
- (4) Sullivan, J. C.; Kalaitzidis, D.; Gilmore, T. D.; Finnerty, J. R. Rel homology domain-containing transcription factors in the cnidarian *Nematostella vectensis*. *Dev. Genes Evol.* **2007**, *217*, 63–72.
- (5) Baldwin, A. S. Control of oncogenesis and cancer therapy resistance by the transcription factor NF-kappaB. *J. Clin. Invest.* **2001**, *107*, 241–246.
- (6) Ghosh, S.; Karin, M. Missing pieces in the NF-kappaB puzzle. *Cell* **2002**, *109 Suppl*, S81–96.
- (7) Gilmore, T. D.; Garbati, M. R. Inhibition of NF-kappaB signaling as a strategy in disease therapy. *Curr. Top. Microbiol. Immunol.* **2011**, *349*, 245–263.
- (8) Gilmore, T. D.; Wolenski, F. S. NF-kappaB: where did it come from and why? *Immunol. Rev.* **2012**, *246*, 14–35.

- (9) Rayet, B.; Gelinas, C. Aberrant Rel/NFkB genes and activity in human cancer. *Oncogene* **1999**, *18*, 6938–6947.
- (10) Gilmore, T. D. Introduction to NF-kappaB: Players, pathways, perspectives. *Oncogene* **2006**, *25*, 6680–6684.
- (11) Perkins, N. D.; Gilmore, T. D. Good cop, bad cop: The different faces of NF-kappaB. *Cell Death Differ.* **2006**, *13*, 759–772.
- (12) Gilmore, T. D.; Gerondakis, S. The c-Rel transcription factor in development and disease. *Genes Cancer* **2011**, *2*, 695–711.
- (13) Gilmore, T. D.; Kalaitzidis, D.; Liang, M. C.; Starczynowski, D. T. The c-Rel transcription factor and B-cell proliferation: A deal with the devil. *Oncogene* **2004**, *23*, 2275–2286.
- (14) Gilmore, T. D. Introduction: The Rel/NF-kappaB signal transduction pathway. *Semin. Cancer Biol.* **1997**, *8*, 61–62.
- (15) Gilmore, T. D.; Koedood, M.; Piffat, K. A.; White, D. W. Rel/NF-kappaB/IkappaB proteins and cancer. *Oncogene* **1996**, *13*, 1367–1378.
- (16) Gilmore, T. D. NF-kappa B, KBF1, dorsal, and related matters. *Cell* **1990**, *62*, 841–843.
- (17) Sun, S. C. Non-canonical NF-kappaB signaling pathway. *Cell Res.* **2011**, *21*, 71–85.
- (18) Beg, A. A.; Ruben, S. M.; Scheinman, R. I.; Haskill, S.; Rosen, C. A.; Baldwin, A. S., Jr. I kappa B interacts with the nuclear localization sequences of the subunits of NF-kappa B: A mechanism for cytoplasmic retention. *Genes Dev.* **1992**, *6*, 1899–1913.
- (19) Beg, A. A.; Baldwin, A. S., Jr. The I kappa B proteins: Multifunctional regulators of Rel/NF-kappa B transcription factors. *Genes Dev.* **1993**, *7*, 2064–2070.
- (20) Zabel, U.; Henkel, T.; Silva, M. S.; Baeuerle, P. A. Nuclear uptake control of NF-kappa B by MAD-3, an I kappa B protein present in the nucleus. *EMBO J.* **1993**, *12*, 201–211.
- (21) Huguet, C.; Crepieux, P.; Laudet, V. Rel/NF-kappa B transcription factors and I kappa B inhibitors: Evolution from a unique common ancestor. *Oncogene* **1997**, *15*, 2965–2974.
- (22) Baeuerle, P. A.; Henkel, T. Function and activation of NF-kappa B in the immune system. *Annu. Rev. Immunol.* **1994**, *12*, 141–179.
- (23) Siebenlist, U.; Franzoso, G.; Brown, K. Structure, regulation and function of NF-kappa B. *Annu. Rev. Cell Biol.* **1994**, *10*, 405–455.
- (24) Karin, M. How NF-kappaB is activated: The role of the IkappaB kinase (IKK) complex. *Oncogene* **1999**, *18*, 6867–6874.
- (25) Israel, A. The IKK complex, a central regulator of NF- $\kappa$ B activation. *Cold Spring Harbor Perspect. Biol.* **2010**, *2*, a000158-1–a000158-14.
- (26) Nishikori, M. Classical and alternative NF- $\kappa$ B activation pathways and their roles in lymphoid malignancies. *J. Clin. Exp. Hematol.* **2005**, *45*, 15–24.
- (27) Gamble, C.; McIntosh, K.; Scott, R.; Ho, K. H.; Plevin, R.; Paul, A. Inhibitory kappa B Kinases as targets for pharmacological regulation. *Br. J. Pharmacol.* **2012**, *165*, 802–819.
- (28) Karin, M.; Delhase, M. The I kappa B kinase (IKK) and NF-kappa B: Key elements of proinflammatory signalling. *Semin. Immunol.* **2000**, *12*, 85–98.
- (29) May, M. J.; Ghosh, S. Rel/NF- $\kappa$ B and I $\kappa$ B proteins: An overview. *Semin. Cancer Biol.* **1997**, *8*, 63–73.
- (30) Zandi, E.; Rothwarf, D. M.; Delhase, M.; Hayakawa, M.; Karin, M. The IkappaB kinase complex (IKK) contains two kinase subunits, IKKalpha and IKKbeta, necessary for IkappaB phosphorylation and NF-kappaB activation. *Cell* **1997**, *91*, 243–252.
- (31) Hacker, H.; Karin, M. Regulation and function of IKK and IKK-related kinases. *Sci. Signaling* **2006**, re13.
- (32) Mercurio, F.; Zhu, H.; Murray, B. W.; Shevchenko, A.; Bennett, B. L.; Li, J.; Young, D. B.; Barbosa, M.; Mann, M.; Manning, A.; Rao, A. IKK-1 and IKK-2: Cytokine-activated IkappaB kinases essential for NF-kappaB activation. *Science* **1997**, *278*, 860–866.
- (33) Hayden, M. S.; Ghosh, S. Signaling to NF-kappaB. *Genes Dev.* **2004**, *18*, 2195–2224.
- (34) Zandi, E.; Chen, Y.; Karin, M. Direct phosphorylation of IkappaB by IKKalpha and IKKbeta: Discrimination between free and NF-kappaB-bound substrate. *Science* **1998**, *281*, 1360–1363.

- (35) Delhase, M.; Karin, M. The I kappa B kinase: a master regulator of NF-kappa B, innate immunity, and epidermal differentiation. *Cold Spring Harbor Symp. Quant. Biol.* **1999**, *64*, 491–503.
- (36) Johnson, L. N.; Noble, M. E.; Owen, D. J. Active and inactive protein kinases: Structural basis for regulation. *Cell* **1996**, *85*, 149–158.
- (37) Pandey, M. K.; Sung, B.; Kunnumakkara, A. B.; Sethi, G.; Chaturvedi, M. M.; Aggarwal, B. B. Berberine modifies cysteine 179 of IkappaBalpha kinase, suppresses nuclear factor-kappaB-regulated antiapoptotic gene products, and potentiates apoptosis. *Cancer Res.* **2008**, *68*, 5370–5379.
- (38) Gupta, S. C.; Prasad, S.; Reuter, S.; Kannappan, R.; Yadav, V. R.; Ravindran, J.; Hema, P. S.; Chaturvedi, M. M.; Nair, M.; Aggarwal, B. B. Modification of cysteine 179 of IkappaBalpha kinase by nimbolide leads to down-regulation of NF-kappaB-regulated cell survival and proliferative proteins and sensitization of tumor cells to chemotherapeutic agents. *J. Biol. Chem.* **2010**, *285*, 35406–35417.
- (39) Byun, M. S.; Choi, J.; Jue, D. M. Cysteine-179 of IkappaB kinase beta plays a critical role in enzyme activation by promoting phosphorylation of activation loop serines. *Exp. Mol. Med.* **2006**, *38*, 546–552.
- (40) Harikumar, K. B.; Kunnumakkara, A. B.; Ahn, K. S.; Anand, P.; Krishnan, S.; Guha, S.; Aggarwal, B. B. Modification of the cysteine residues in IkappaBalpha kinase and NF-kappaB (p65) by xanthohumol leads to suppression of NF-kappaB-regulated gene products and potentiation of apoptosis in leukemia cells. *Blood* **2009**, *113*, 2003–2013.
- (41) Xu, G.; Lo, Y. C.; Li, Q.; Napolitano, G.; Wu, X.; Jiang, X.; Dreano, M.; Karin, M.; Wu, H. Crystal structure of inhibitor of kappaB kinase beta. *Nature* **2011**, *472*, 325–330.
- (42) Nolen, B.; Taylor, S.; Ghosh, G. Regulation of protein kinases; controlling activity through activation segment conformation. *Mol. Cell* **2004**, *15*, 661–675.
- (43) Boutros, T.; Chevet, E.; Metrakos, P. Mitogen-activated protein (MAP) kinase/MAP kinase phosphatase regulation: Roles in cell growth, death, and cancer. *Pharmacol. Rev.* **2008**, *60*, 261–310.
- (44) Pearson, G.; Robinson, F.; Beers Gibson, T.; Xu, B. E.; Karandikar, M.; Berman, K.; Cobb, M. H. Mitogen-activated protein (MAP) kinase pathways: Regulation and physiological functions. *Endocr. Rev.* **2001**, *22*, 153–183.
- (45) Dhillon, A. S.; Hagan, S.; Rath, O.; Kolch, W. MAP kinase signalling pathways in cancer. *Oncogene* **2007**, *26*, 3279–3290.
- (46) Ferrell, J. E., Jr.; Bhatt, R. R. Mechanistic studies of the dual phosphorylation of mitogen-activated protein kinase. *J. Biol. Chem.* **1997**, *272*, 19008–19016.
- (47) Kalia, M.; Kukol, A. Structure and dynamics of the kinase IKK-beta—A key regulator of the NF-kappa B transcription factor. *J. Struct. Biol.* **2011**, *176*, 133–142.
- (48) Kornev, A. P.; Taylor, S. S.; Ten Eyck, L. F. A helix scaffold for the assembly of active protein kinases. *Proc. Natl. Acad. Sci. U.S.A.* **2008**, *105*, 14377–14382.
- (49) Steichen, J. M.; Iyer, G. H.; Li, S.; Saldanha, S. A.; Deal, M. S.; Woods, V. L., Jr.; Taylor, S. S. Global consequences of activation loop phosphorylation on protein kinase A. *J. Biol. Chem.* **2010**, *285*, 3825–3832.
- (50) Scheeff, E. D.; Bourne, P. E. Structural evolution of the protein kinase-like superfamily. *PLoS Comput. Biol.* **2005**, *1*, e49–1–e49–23.
- (51) Zuccotto, F.; Ardini, E.; Casale, E.; Angiolini, M. Through the “gatekeeper door”: Exploiting the active kinase conformation. *J. Med. Chem.* **2010**, *53*, 2681–2694.
- (52) Palermo, N. Y.; Natarajan, A. Beyond the frog: The evolution of homology models of human IKKbeta. *Bioorg. Med. Chem. Lett.* **2011**, *21*, 6081–6084.
- (53) Berman, H. M. The Protein Data Bank. *Nucleic Acids Res.* **2000**, *28*, 235–242.
- (54) *Molecular Operating Environment (MOE)*, 2011.10; Chemical Computing Group Inc.: Montreal, Quebec, Canada, 2011.
- (55) Wang, J.; Cieplak, P.; Kollman, P. A. How well does a restrained electrostatic potential (RESP) model perform in calculating conformational energies of organic and biological molecules? *J. Comput. Chem.* **2000**, *21*, 1049–1074.
- (56) Ponder, J. W.; Case, D. A. Force fields for protein simulations. *Adv. Protein Chem.* **2003**, *66*, 27–85.
- (57) Salomon-Ferrer, R.; Case, D. A.; Walker, R. C. An overview of the Amber biomolecular simulation package. *Wiley Interdiscip. Rev.: Comput. Mol. Sci.* **2013**, *3*, 198–210.
- (58) Case, D. A.; Cheatham, T. E.; Darden, T.; Gohlke, H.; Luo, R.; Merz, K. M.; Onufriev, A.; Simmerling, C.; Wang, B.; Woods, R. J. The Amber biomolecular simulation programs. *J. Comput. Chem.* **2005**, *26*, 1668–1688.
- (59) Soga, S.; Shirai, H.; Kobori, M.; Hirayama, N. Use of amino acid composition to predict ligand-binding sites. *J. Chem. Inf. Model.* **2007**, *47*, 400–406.
- (60) Durand, E.; Derrez, E.; Audoly, G.; Spinelli, S.; Ortiz-Lombardia, M.; Raoult, D.; Cascales, E.; Cambillau, C. Crystal structure of the VgrG1 actin cross-linking domain of the *Vibrio cholerae* type VI secretion system. *J. Biol. Chem.* **2012**, *287*, 38190–38199.
- (61) Meagher, K. L.; Redman, L. T.; Carlson, H. A. Development of polyphosphate parameters for use with the AMBER force field. *J. Comput. Chem.* **2003**, *24*, 1016–1025.
- (62) Wang, J.; Wolf, R. M.; Caldwell, J. W.; Kollman, P. A.; Case, D. A. Development and testing of a general amber force field. *J. Comput. Chem.* **2004**, *25*, 1157–1174.
- (63) Homeyer, N.; Horn, A. H.; Lanig, H.; Sticht, H. AMBER force-field parameters for phosphorylated amino acids in different protonation states: Phosphoserine, phosphothreonine, phosphotyrosine, and phosphohistidine. *J. Mol. Model.* **2006**, *12*, 281–289.
- (64) Kenzaki, H.; Koga, N.; Hori, N.; Kanada, R.; Li, W.; Okazaki, K.; Yao, X.; Takada, S. CafeMol: A coarse-grained biomolecular simulator for simulating proteins at work. *J. Chem. Theory Comput.* **2011**, *7*, 1979–1989.
- (65) Joung, I. S.; Cheatham, T. E. Determination of alkali and halide monovalent ion parameters for use in explicitly solvated biomolecular simulations. *J. Phys. Chem. B* **2008**, *112*, 9020–9041.
- (66) Berendsen, H. J. C.; Grigera, J. R.; Straatsma, T. P. The missing term in effective pair potentials. *J. Phys. Chem.* **1987**, *91*, 6269–6271.
- (67) Hornak, V.; Abel, R.; Okur, A.; Strockbine, B.; Roitberg, A.; Simmerling, C. Comparison of multiple Amber force fields and development of improved protein backbone parameters. *Proteins* **2006**, *65*, 712–725.
- (68) Pettersen, E. F.; Goddard, T. D.; Huang, C. C.; Couch, G. S.; Greenblatt, D. M.; Meng, E. C.; Ferrin, T. E. UCSF Chimera—a visualization system for exploratory research and analysis. *J. Comput. Chem.* **2004**, *25*, 1605–1612.
- (69) Prall, M. VMD: A graphical tool for the modern chemists. *J. Comput. Chem.* **2001**, *22*, 132–134.
- (70) Miller, B. R.; McGee, T. D.; Swails, J. M.; Homeyer, N.; Gohlke, H.; Roitberg, A. E. MMPBSA.py: An efficient program for end-state free energy calculations. *J. Chem. Theory Comput.* **2012**, *8*, 3314–3321.
- (71) Hawkins, G. D.; Cramer, C. J.; Truhlar, D. G. Pairwise solute descreening of solute charges from a dielectric medium. *Chem. Phys. Lett.* **1995**, *246*, 122–129.
- (72) Hawkins, G. D.; Cramer, C. J.; Truhlar, D. G. Parametrized models of aqueous free energies of solvation based on pairwise descreening of solute atomic charges from a dielectric medium. *J. Phys. Chem.* **1996**, *100*, 19824–19839.
- (73) Tsui, V.; Case, D. A. Theory and applications of the generalized born solvation model in macromolecular simulations. *Biopolymers* **2000**, *56*, 275–291.
- (74) Onufriev, A.; Bashford, D.; Case, D. A. Exploring protein native states and large-scale conformational changes with a modified Generalized Born model. *Proteins: Struct., Funct., Bioinf.* **2004**, *55*, 383–394.
- (75) Massova, I.; Kollman, P. A. Combined molecular mechanical and continuum solvent approach (MM-PBSA/GBSA) to predict ligand binding. *Perspect. Drug Discovery Des.* **2000**, *18*, 113–135.

- (76) Krissinel, E.; Henrick, K. Inference of macromolecular assemblies from crystalline state. *J. Mol. Biol.* **2007**, *372*, 774–797.
- (77) Krissinel, E. Crystal contacts as nature's docking solutions. *J. Comput. Chem.* **2010**, *31*, 133–143.
- (78) Mandal, S.; Moudgil, M.; Mandal, S. K. Rational drug design. *Eur. J. Pharmacol.* **2009**, *625*, 90–100.
- (79) Durrant, J. D.; McCammon, J. A. Molecular dynamics simulations and drug discovery. *BMC Biol.* **2011**, *9*, 71–1–71–9.
- (80) Borhani, D. W.; Shaw, D. E. The future of molecular dynamics simulations in drug discovery. *J. Comput.-Aided Mol. Des.* **2012**, *26*, 15–26.
- (81) Hao, G. F.; Yang, G. F.; Zhan, C. G. Structure-based methods for predicting target mutation-induced drug resistance and rational drug design to overcome the problem. *Drug Discovery Today* **2012**, *17*, 1121–1126.
- (82) Chodera, J. D.; Mobley, D. L.; Shirts, M. R.; Dixon, R. W.; Branson, K.; Pande, V. S. Alchemical free energy methods for drug discovery: progress and challenges. *Curr. Opin. Struct. Biol.* **2011**, *21*, 150–160.
- (83) Mobley, D. L.; Chodera, J. D.; Dill, K. A. The confine-and-release method: Obtaining correct binding free energies in the presence of protein conformational change. *J. Chem. Theory Comput.* **2007**, *3*, 1231–1235.
- (84) Tozzini, V. Minimalist models for proteins: A comparative analysis. *Q. Rev. Biophys.* **2010**, *43*, 333–371.
- (85) Kamerlin, S. C. L.; Vicatos, S.; Dryga, A.; Warshel, A. Coarse-Grained (multiscale) simulations in studies of biophysical and chemical systems. *Annu. Rev. Phys. Chem.* **2011**, *62*, 41–64.
- (86) Li, F.; Gangal, M.; Juliano, C.; Gorfain, E.; Taylor, S. S.; Johnson, D. A. Evidence for an internal entropy contribution to phosphoryl transfer: a study of domain closure, backbone flexibility, and the catalytic cycle of cAMP-dependent protein kinase. *J. Mol. Biol.* **2002**, *315*, 459–469.
- (87) Li, F.; Gangal, M.; Jones, J. M.; Deich, J.; Lovett, K. E.; Taylor, S. S.; Johnson, D. A. Consequences of cAMP and catalytic-subunit binding on the flexibility of the A-kinase regulatory subunit. *Biochemistry* **2000**, *39*, 15626–15632.
- (88) Polley, S.; Huang, D.; Hauenstein, A. V.; Fusco, A. J.; Zhong, X.; Vu, D.; Schroefelbauer, B.; Kim, Y.; Hoffmann, A.; Verma, I. M.; Ghosh, G.; Huxford, T. A structural basis for I $\kappa$ B kinase 2 activation via oligomerization dependent trans auto-phosphorylation. *PLoS Biol.* **2013**, *11*, e1001581–1–e1001581–13.
- (89) Liu, S.; Misquitta, Y. R.; Olland, A.; Johnson, M. A.; Kelleher, K. S.; Kriz, R.; Lin, L. L.; Stahl, M.; Mosyak, L. Crystal structure of a human IkappaB kinase beta asymmetric dimer. *J. Biol. Chem.* **2013**, *288*, 22758–22767.